LA-UR-16-23742
Approved for public release; distribution is unlimited.

Title: Demonstration of finite element simulations in MOOSE using crystallographic models of irradiation hardening and plastic deformation

Author(s): Patra, Anirban
Wen, Wei
Martinez Saez, Enrique
Tome, Carlos

Intended for: Report

Issued: 2016-05-27

Demonstration of finite element simulations in MOOSE using crystallographic models of irradiation hardening and plastic deformation

Anirban Patra, Wei Wen, Enrique Martínez, Carlos N. Tomé

Materials Science and Technology Division, Los Alamos National Laboratory

Los Alamos, NM 87545

Report on Milestone:

M3MS-16LA0501034: Interface hardening models with MOOSE-BISON-MARMOT

May 31, 2016

Demonstration of finite element simulations in MOOSE using crystallographic models of irradiation hardening and plastic deformation

Anirban Patra, Wei Wen, Enrique Martínez, Carlos N. Tomé

Materials Science and Technology Division, Los Alamos National Laboratory

Los Alamos, NM 87545

1. Introduction

This report describes the implementation of a crystal plasticity framework (VPSC) for irradiation hardening and plastic deformation in the finite element code, MOOSE. Constitutive models for irradiation hardening and the crystal plasticity framework are described in a previous report [1]. Here we describe these models briefly and then describe an algorithm for interfacing VPSC with finite elements. Example applications of tensile deformation of a dog bone specimen and a 3D pre-irradiated bar specimen performed using MOOSE are demonstrated.

2. Constitutive Model Description

The constitutive model framework, adopted from [2], [3], is described in detail in Ref. [1]. We will briefly summarize it here.

The following internal state variables (ISVs) are used at the level of slip system, κ, in our crystal plasticity framework: mobile dislocation density, ρ_M^κ, immobile dislocation density, ρ_I^κ, number density, N_{111}^κ, and size, d_{111}^κ, of <111> dislocation loops, number density, N_{100}^κ, and size, d_{100}^κ, of <100> dislocation loops, and number density, $N_{\alpha'}^\kappa$, and size, $d_{\alpha'}^\kappa$, of α' precipitates.

The crystallographic shearing rate, $\dot{\gamma}^\kappa$, is given as a function of the resolved shear stress, τ^κ, such that:

$$\dot{\gamma}^\kappa = \dot{\gamma}_0 \left(\frac{\left|\tau^\kappa\right|}{\tau_0^\kappa} \right)^n \operatorname{sgn}\left(\tau^\kappa\right) \tag{1}$$

where, $\dot{\gamma}_0$ is the reference shear rate, τ_0^κ is the slip resistance, and n is the inverse of strain rate sensitivity.

The contributions to slip resistance, τ_0^κ, are assumed to be: the intrinsic frictional resistance, σ_0, the Hall-Petch term accounting for grain size dependence [4], [5], $\sigma_{HP} = k_{HP} / \sqrt{D}$ (k_{HP} is a material constant, D is the grain size), and the lattice resistance to dislocation glide due to long range interactions, σ_{LR}^κ, with other dislocations, dislocation loops, and α' precipitates. A dispersed barrier hardening model [6], [7] is used to model these long range interactions, such that:

$$\sigma_{LR}^{\kappa}=Gb\left(h_{\rho}\sqrt{\sum_{\zeta}A_{\kappa\zeta}\left(\rho_M^{\zeta}+\rho_I^{\zeta}\right)}+h_{111}\sqrt{N_{111}^{\kappa}d_{111}^{\kappa}}+h_{111}\sqrt{N_{100}^{\kappa}d_{100}^{\kappa}}+h_{\alpha'}\sqrt{N_{\alpha'}^{\kappa}d_{\alpha'}^{\kappa}}\right) \tag{2}$$

where, G is the shear modulus, b is the Burgers vector magnitude, $A_{\kappa\zeta}$ is the matrix of slip system dislocation interaction coefficients (to model self and latent hardening), and h_{ρ}, h_{111}, h_{100}, $h_{\alpha'}$ are the hardening coefficients associated with line dislocations, <111> dislocation loops, <100> dislocation loops, and α' precipitates, respectively.

Accordingly, the total slip resistance on slip system, κ, has the following form:

$$\tau_0^{\kappa}=\sigma_0+\sigma_{HP}+\sigma_{LR}^{\kappa} \tag{3}$$

Mobile dislocations are assumed to evolve primarily via three mechanisms [2]: creation of mobile dislocations via multiplication at existing dislocation segments, mutual annihilation of dislocation dipoles, and trapping of mobile dislocation segments at barriers, thus rendering them immobile. Dynamic recovery of immobile dislocations may lead to the depletion of the immobile dislocation population. Accordingly, the net rate of evolution of mobile and immobile dislocations is given as

$$\dot{\rho}_M^{\kappa}=\frac{k_{mul}}{bl_d}\left|\dot{\gamma}^{\kappa}\right|-\frac{2R_c}{b}\rho_M^{\kappa}\left|\dot{\gamma}^{\kappa}\right|-\frac{1}{b\lambda^{\kappa}}\left|\dot{\gamma}^{\kappa}\right| \tag{4}$$

$$\dot{\rho}_I^{\kappa}=\frac{1}{b\lambda^{\kappa}}\left|\dot{\gamma}^{\kappa}\right|-k_{dyn}\rho_I^{\kappa}\left|\dot{\gamma}^{\kappa}\right| \tag{5}$$

where, k_{mul} is a material constant associated with dislocation multiplication, $l_d=1/\sqrt{\sum_{\zeta}\rho_M^{\zeta}+\rho_I^{\zeta}+N_{111}^{\zeta}d_{111}^{\zeta}+N_{100}^{\zeta}d_{100}^{\zeta}}$ is the total line length of dislocations [8], R_c is the capture radius associated with mutual annihilation of mobile dislocations (the factor of 2 accounts for the fact that two dislocations are annihilated during this event) [9], λ^{κ} is the effective mean free path of trapping mobile dislocations at barriers, given by [10], [11]

$$\frac{1}{\lambda^{\kappa}}=\frac{1}{\lambda_{\rho}^{\kappa}}+\frac{1}{\lambda_{111}^{\kappa}}+\frac{1}{\lambda_{100}^{\kappa}}+\frac{1}{\lambda_{\alpha'}^{\kappa}}=\beta_{\rho}\sqrt{\rho_M^{\kappa}+\rho_I^{\kappa}}+\beta_{111}\sqrt{N_{111}^{\kappa}d_{111}^{\kappa}}+\beta_{100}\sqrt{N_{100}^{\kappa}d_{100}^{\kappa}}+\beta_{\alpha'}\sqrt{N_{\alpha'}^{\kappa}d_{\alpha'}^{\kappa}} \tag{6}$$

and k_{dyn} is the material constant associated with dynamic recovery. β_{ρ}, β_{111}, β_{100}, and $\beta_{\alpha'}$ are the trapping coefficients associated with line dislocations, <111> dislocation loops, <100> dislocation loops, and α' precipitates, respectively. Detailed description of the physical mechanisms behind these models is given in Ref. [1], [2].

The interaction of irradiation-induced defects with mobile dislocations is modeled using a previously developed phenomenological model [3] that accounts for the annihilation rate of irradiation-induced defects as a function of the crystallographic defect density and the interacting mobile dislocation density. Accordingly, the rate of annihilation of the areal density of irradiation-induced defects is given as [3]

$$\dot{N}_{111}^{\kappa} d_{111}^{\kappa} = -\frac{R_{111}^{\kappa}}{b} \left(N_{111}^{\kappa} d_{111}^{\kappa} \right)^{c} \left(\rho_{M}^{\kappa} \right)^{1-c} \left| \dot{\gamma}^{\kappa} \right| \quad (7)$$

$$\dot{N}_{100}^{\kappa} d_{100}^{\kappa} = -\frac{R_{100}^{\kappa}}{b} \left(N_{100}^{\kappa} d_{100}^{\kappa} \right)^{c} \left(\rho_{M}^{\kappa} \right)^{1-c} \left| \dot{\gamma}^{\kappa} \right| \quad (8)$$

$$\dot{N}_{\alpha'}^{\kappa} d_{\alpha'}^{\kappa} = -\frac{R_{\alpha'}^{\kappa}}{b} \left(N_{\alpha'}^{\kappa} d_{\alpha'}^{\kappa} \right)^{c} \left(\rho_{M}^{\kappa} \right)^{1-c} \left| \dot{\gamma}^{\kappa} \right| \quad (9)$$

where, c is the annihilation exponent, and R_{111}^{κ} , R_{100}^{κ} , and $R_{\alpha'}^{\kappa}$ are the capture radii associated with the annihilation of <111> loops, <100> loops, and α' precipitates, respectively.

3. Polycrystal Framework

The visco-plastic self-consistent (VPSC) framework is used to relate the macroscopic polycrystal deformation to the individual grains deformation. The self-consistent model assumes that each grain can be considered as an inhomogeneous inclusion embedded in an effective medium having the average properties of all grains in the aggregate. A detailed description of the VPSC model can be found in Refs. [12], [13]. Plastic deformation in each grain occurs via the activation of slip and/or twin systems. The total strain rate on a given grain is given by the combined contribution of the shear rates of all slip and twinning systems, and the latter are related to the stress in the grain through the constitutive law:

$$\dot{\varepsilon}_{ij}^{g} = \sum_{s} m_{ij}^{s} \dot{\gamma}^{s} = \dot{\gamma}_{0} \sum_{s} m_{ij}^{s} \left(\frac{m_{kl}^{s} : \sigma_{kl}^{g}}{\tau^{s}} \right)^{n} \quad (10)$$

where, $m_{ij}^{s} = \frac{1}{2}\left(n_{i}^{s} b_{j}^{s} + n_{j}^{s} b_{i}^{s} \right)$ is the symmetric Schmid tensor associated with slip system s; $\overline{n}^{s}$ and $\overline{b}^{s}$ are the normal and burgers vector of the system; $\dot{\varepsilon}_{ij}^{g}$ and σ_{kl}^{g} are the deviatoric strain-rate and stress of the grain, $\dot{\gamma}_{0}$ is the normalization rate and n is the rate sensitivity exponent. The linearized form for the constitutive law of the single crystal response is:

$$\dot{\varepsilon}_{ij}^{g} = M_{ijkl}^{g} \left(\sigma^{g} \right) \sigma_{kl}^{g} + \dot{\varepsilon}_{ij}^{0,g} \quad (11)$$

where, M_{ijkl}^{g} and $\dot{\varepsilon}_{ij}^{0,g}$ are the visco-plastic compliance and the back-extrapolated rate of grain g, respectively. Depending on the linearization assumption chosen, Eq. (11) gives a response that goes from the stiff secant to the compliant tangent approximation [12]. For an affine linearization (the kind used in the present work), the actual grain level compliance is used, i.e.,

$$M^{g}_{ijkl} = n\dot{\gamma}_0 \sum_s \frac{m^s_{ij} m^s_{kl}}{\tau^0_s} \left(\frac{m^s_{pq} \sigma^g_{pq}}{\tau^0_s} \right)^{n-1} \tag{12}$$

$$\dot{\varepsilon}^{0,g}_{ij} = (1-n)\,\dot{\varepsilon}^{g} \tag{13}$$

Performing homogenization on this linearized heterogeneous medium consists of assuming that a linear relation analogous to Eq. (13) is valid at the effective medium (polycrystal) level:

$$\bar{\dot{\varepsilon}}_{ij} = \bar{M}_{ijkl}(\bar{\sigma})\,\bar{\sigma}_{kl} + \bar{\dot{\varepsilon}}^{0}_{ij} \tag{14}$$

where, $\bar{\dot{\varepsilon}}_{ij}$ and $\bar{\sigma}_{kl}$ are the macroscopic rate and stress, and $\bar{M}_{ijkl}$ and $\bar{\dot{\varepsilon}}^{0}_{ij}$ are the macroscopic viscoplastic compliance and back extrapolated rate, respectively. Solving the stress equilibrium equation of an ellipsoidal inclusion described by Eq. (11) embedded in a medium described by Eq. (14) leads to the so called 'interaction equation' relating macroscopic and inclusion magnitudes

$$(\dot{\varepsilon}_{ij} - \bar{\dot{\varepsilon}}_{ij}) = -\tilde{M}_{ijkl}\,(\sigma_{kl} - \bar{\sigma}_{kl}) \tag{15}$$

where,

$$\tilde{M}_{ijkl} = (I - S)^{-1}_{ijmn}\, S_{mnpq}\, \bar{M}_{pqkl} \tag{16}$$

is the 'interaction tensor'. Depending on the linearization assumption chosen, $\bar{M}$ varies between the upper bound compliance $\bar{M}^{\text{tangent}}$ and the lower bound compliance, $\bar{M}^{\text{secant}} = \bar{M}^{\text{tangent}}/n$.

The macroscopic moduli are unknown *a priori* and need to be adjusted self-consistently by enforcing the condition that the average stress and strain rate over all grains has to be equal to the macroscopic stress and strain rate:

$$\bar{\dot{\varepsilon}}_{ij} = \langle \dot{\varepsilon}_{ij} \rangle, \quad \sigma_{ij} = \langle \sigma_{ij} \rangle \tag{17}$$

The conditions in Eq. (17), along with grain strain rate and stress given by the visco-plastic inclusion formalism, define what is called a 'self-consistent visco-plastic' polycrystal model. Substituting Eqs. (11) and (14) in Eq. (17) leads to an expression for the visco-plastic moduli of the linearized effective medium [12].

4. VPSC-Finite Element Interface

In this work, the constitutive deformation behavior of the FEs is solved at the level of grains using VPSC. Effectively, each Gauss point in the FE mesh represents a polycrystalline aggregate with associated texture. VPSC solves the local boundary conditions imposed by the interface code between VPSC and FE (referred as VPSC-FE interface from here on) and then passes the deformed (stress and strain) state of the Gauss point to the FE code, which solves for global equilibrium of deformation in the FE mesh.

VPSC has previously been interfaced with the FE code, ABAQUS [14], and implemented in the form of a User MATerial subroutine (UMAT) [15], [16], and also with the BISON-CASL fuel performance code in the form of a material model [17]. In this work, a similar algorithm has been used, albeit with a modified convergence criterion.

VPSC has been interfaced with MOOSE to simulate component-level irradiation growth and creep in Zr alloys (under the CASL program) [18]. Here the same algorithm is used and is briefly explained in the following. Before moving forward, it should be noted that standalone VPSC only solves for the viscoplastic strain corresponding to a stress state (or, vice-versa) and does not model the elastic strain. The VPSC-FE interface described here accounts for 'macroscopic' elastic deformation as well. Also note that VPSC solves for deformation in the local (material) coordinate system, which is then rotated to the global (component level) coordinate system for FE calculations.

An additive decomposition of the strain increment, $\Delta\boldsymbol{\varepsilon}$, into the elastic, $\Delta\boldsymbol{\varepsilon}^{e}$, and viscoplastic, $\Delta\boldsymbol{\varepsilon}^{vp}$, parts is assumed in the VPSC-FE interface, i.e., $\Delta\boldsymbol{\varepsilon} = \Delta\boldsymbol{\varepsilon}^{e} + \Delta\boldsymbol{\varepsilon}^{vp}$. The stress increment, $\Delta\boldsymbol{\sigma}$, corresponding to this strain increment may be used to estimate the elastic strain increment, i.e., $\Delta\boldsymbol{\varepsilon}^{e} = \boldsymbol{C}^{-1} : \Delta\boldsymbol{\sigma}$, where $\boldsymbol{C}$ is the self-consistent elastic stiffness of the polycrystalline aggregate calcualted by the VPSC code at the beginning of each deformation increment. The history-dependent viscoplastic strain increment, $\Delta\boldsymbol{\varepsilon}^{vp}$, on the other hand, is a function of the stress state, $\boldsymbol{\sigma}$ (rather than the stress increment), and the internal state variables (ISVs) in the constitutive model.

The FE code calls the VPSC-FE interface with an estimate of the stretch increment, $\Delta\boldsymbol{\varepsilon}_{FE}$, the rigid spin increment, $\Delta\boldsymbol{R}_{FE}$, and the time step increment, Δt. The VPSC-FE interface then solves for $\boldsymbol{\sigma}$ corresponding to this strain increment using an iterative Newton-Raphson scheme. The trial stress at time, $t+\Delta t$, is estimated based on the elastic strain increment from the previous time step, i.e.,

$$\boldsymbol{\sigma}_{t+\Delta t} = \boldsymbol{\sigma}_{t} + \Delta\boldsymbol{\sigma} = \boldsymbol{\sigma}_{t} + \boldsymbol{C} : \Delta\boldsymbol{\varepsilon}^{e} = \boldsymbol{\sigma}_{t} + \boldsymbol{C} : \left(\Delta\boldsymbol{\varepsilon} - \Delta\boldsymbol{\varepsilon}^{vp}\right) \tag{18}$$

where, the subscript refers to the respective time increment. VPSC is called with this stress state, $\boldsymbol{\sigma}_{t+\Delta t}$, to obtain the corresponding viscoplastic strain rate, $\dot{\boldsymbol{\varepsilon}}^{vp}$. VPSC-FE interface then calculates the residual between $\Delta\boldsymbol{\varepsilon}$ and $\Delta\boldsymbol{\varepsilon}_{FE}$ according to the following expression:

$$\boldsymbol{X}\left(\Delta\boldsymbol{\sigma}\right) = \Delta\boldsymbol{\varepsilon} - \Delta\boldsymbol{\varepsilon}_{FE} = \boldsymbol{C}^{-1} : \Delta\boldsymbol{\sigma} + \dot{\boldsymbol{\varepsilon}}^{vp}\Delta t - \Delta\boldsymbol{\varepsilon}_{FE} \tag{19}$$

If the convergence criteria (described in the following) is not satisfied in increment k, a trial stress increment for the next iteration, $k+1$, is calculated as

$$\left(\Delta\boldsymbol{\sigma}\right)_{k+1} = \left(\Delta\boldsymbol{\sigma}\right)_{k} - \boldsymbol{J}_{NR}^{-1}\left(\left(\Delta\boldsymbol{\sigma}\right)_{k}\right) : \boldsymbol{X}\left(\left(\Delta\boldsymbol{\sigma}\right)_{k}\right) \tag{20}$$

where, the Jacobian, $\boldsymbol{J}_{NR}$, of the Newton-Raphson iteration is given as

$$\boldsymbol{J}_{NR}\left(\Delta\boldsymbol{\sigma}\right) = \frac{\partial \boldsymbol{X}\left(\Delta\boldsymbol{\sigma}\right)}{\partial\left(\Delta\boldsymbol{\sigma}\right)} = \boldsymbol{C}^{-1} + \boldsymbol{M}\Delta t \tag{21}$$

where, $\boldsymbol{M}$ is the viscoplastic tangent moduli computed by VPSC as part of the self-consistent calculations.

A weighted convergence metric (cf. [19]) is employed here to achieve faster convergence. The scalar convergence metric is weighted according to the largest component of the strain increment, $\Delta\boldsymbol{\varepsilon}_{FE}$, such that

$$\chi = \sqrt{\sum_{i}\sum_{j}\left(\frac{\left|\Delta\varepsilon_{FE}^{ij}\right|}{\max\left(\left|\Delta\varepsilon_{FE}^{ij}\right|\right)} X^{ij}\right)^{2}} \tag{22}$$

where, i and j denote the respective indices of the tensor quantities.

Note that VPSC computes all quantities in the local coordinate system (the one in which the texture of the cladding is referred to), while the FE code computes all quantities in the global coordinate system. The VPSC-FE interface, therefore, rotates all deformation quantities from the global to the local coordinate system via the rotation tensor, $\boldsymbol{R} = \Delta\boldsymbol{R}_{FE} \cdot \boldsymbol{R}_{t}$ before passing them from the FE code on to VPSC (and, vice-versa). Also note that the tangent stiffness matrix, $\boldsymbol{C}^{t}$, required by some FE codes for calculation of the deformation increment for the next time step, is simply the inverse of the Jacobian used in the Newton-Raphson calculations in Eq. (21), i.e, $\boldsymbol{C}^{t} = \boldsymbol{J}_{NR}^{-1}$. This is therefore passed on to the calling FE code by VPSC-FE interface. The algorithm for interfacing VPSC with the FE code is summarized in Fig. 1 [18].

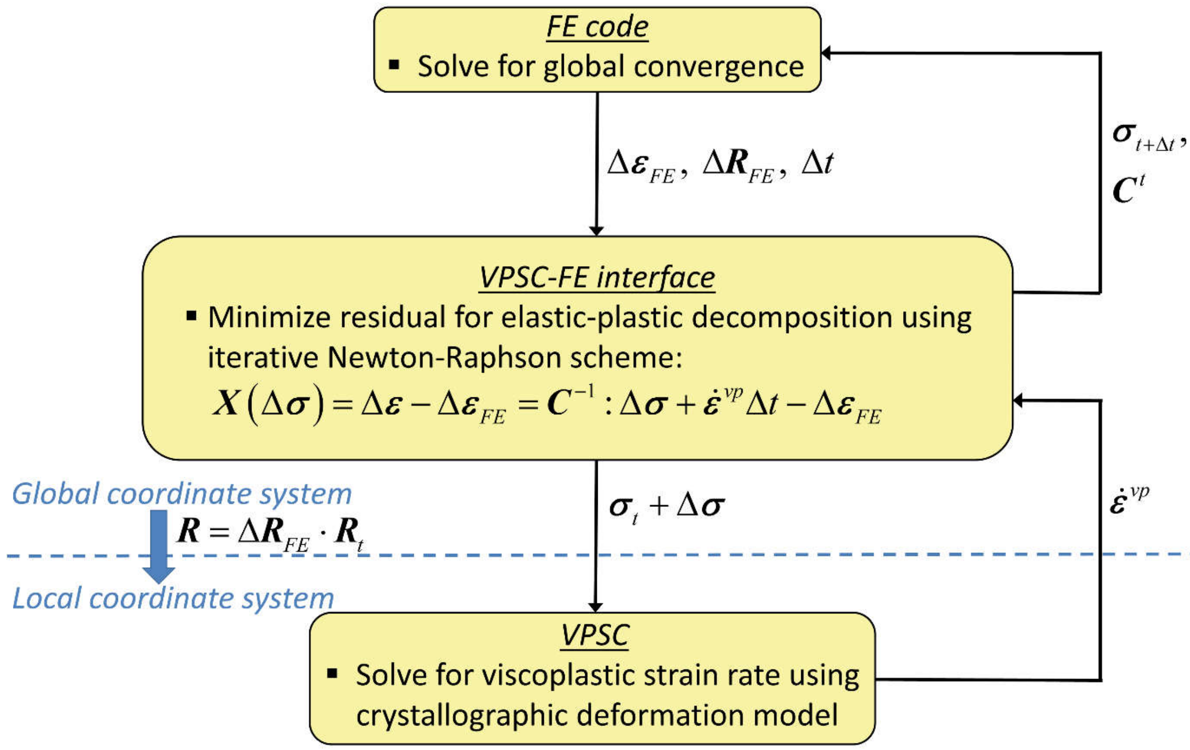

Figure 1. Algorithm for interfacing VPSC with the FE code (from *[18]*).

4. Model Application

The VPSC-FE interface code has been implemented in a general fashion such that it can be used with ABAQUS and MOOSE FE codes (an additional wrapper code is implemented to call the VPSC-FE interface from MOOSE). This allows for benchmarking model predictions of the deformation behavior across different FE codes.

4.1. Benchmarking VPSC-FE predictions with VPSC standalone predictions

We performed single element simulations in MOOSE to compare model predictions with VPSC standalone (referred as VPSC-SA here on) predictions. Symmetric boundary conditions were imposed and the simulation geometry was loaded in tension to 0.1 true strain at a strain rate of 10^{-3} s^{-1}, as in the VPSC-SA calculations. Figure 2 compares the true stress-strain curves from VPSC-FE and VPSC-SA calculations for two different materials: (a) unirradiated Fe-15Cr-4Al weld zone material, representative of an annealed material, and (b) Fe-15Cr-3.9Al alloy irradiated to 1.6 dpa (cf. [20], [21]). The material models were calibrated to the experimental stress-strain response and yield stress in the previous phase of this project (cf. [1]). An initial texture representative of a randomly oriented polycrystal with 50 orientations (shown in Fig. 3) was used in these calculations.

As seen in Fig. 2, a reasonable agreement is obtained between predictions from VPSC-FE and VPSC-SA calculations. As mentioned earlier, VPSC-SA does not account for elastic deformation. This leads to the discrepancy observed between VPSC-FE and VPSC-FE predictions, especially at very low strains (< 0.005). Once plastic deformation commences, VPSC-FE predicts a marginally lower true stress at a given strain for both materials. This is due to the fact that VPSC-FE accommodates the imposed strain via both elastic and plastic deformation. At a given strain, relatively lower plastic strain in the VPSC-FE simulations (as compared to VPSC-SA calculations) leads to lower hardening and lower flow stress. However, the difference in predictions between the two calculations is less than 1% and compare favorably.

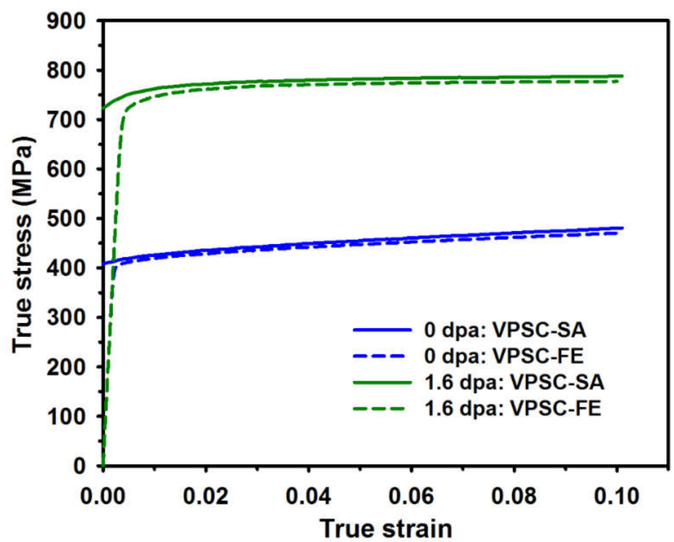

Figure 2. Model predictions of true stress-strain response from VPSC-SA and VPSC-FE calculations for two different FeCrAl alloys.

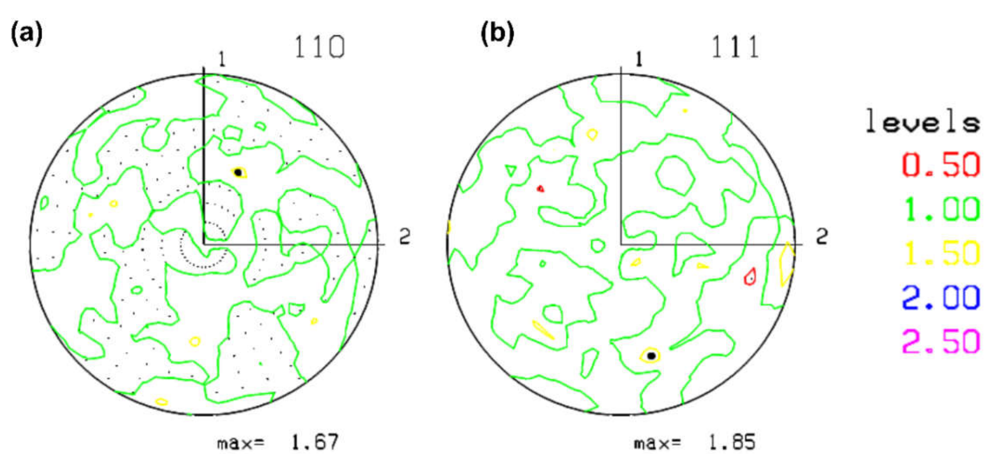

Figure 3. Initial texture used for VPSC-FE and VPSC-SA model comparisons using 50 randomly oriented grains.

4.2. Tensile deformation of a dog bone specimen

We have simulated tensile deformation in the half-geometry of a dog bone specimen using the VPSC-FE interface in MOOSE. Dimensions of the half-geometry of the tensile specimen used in our FE simulations is shown in Fig. 4 and were taken from Ref. [21], where they were used to determine the tensile properties of various FeCrAl alloys. The total length of the specimen is 16 mm. The gage length is 5 mm and the grip length is 4.1 mm. The gage width is 1.2 mm and the grip width is 4 mm. The thickness of the specimen is 0.75 mm. The half-geometry was meshed using 5390 elements with a minimum element size of 0.15 mm. The bottom face of the specimen was constrained along the y-direction. The flat face of the half-geometry was constrained along the x-direction along the length of the specimen. The bottom corner edge of the specimen was constrained in all degrees of freedom to prevent rigid body motion. Displacement-controlled tensile loading was applied on the top face along the y-direction at a rate of 0.016 $mm \cdot s^{-1}$, effectively implying a nominal strain rate of 10^{-3} s^{-1}. The material is representative of an unirradiated Fe-15Cr-4Al weld zone alloy. A randomly instantiated texture with 10 orientations was used in this simulation and is shown in Fig. 5. Model parameters used in these simulations are given in Ref. [1].

Figure 6 shows the distribution of strain along the y-direction and the corresponding von Mises stress in the specimen after loading the specimen in tension for 60 s. As expected, majority of the deformation takes place in the gage section of the specimen. The gage section exhibits strain magnitudes as high as 19%, while the grips generally exhibit strain magnitudes lower than 1%. This is also evident from the distribution of the von Mises effective stress across the length of the specimen. A representative stress-strain response from an element picked at random near the center of the section of the gage section is shown in Fig. 7. Note that this material, with 10 orientations, is 'more textured' (Fig. 5) as compared to the random polycrystal (Fig. 3), with 50 orientations. As a result, this tensile specimen exhibits a higher flow stress ($\approx$ 35 MPa) and hardening as compared to the corresponding unirradiated Fe-15Cr-4Al weld zone alloy in Fig. 2. Less number of orientations were used in these simulations simply to minimize computational costs at the level of VPSC calculations. However, this highlights the importance of having an appropriate reduced texture that is representative of the processing history of the material.

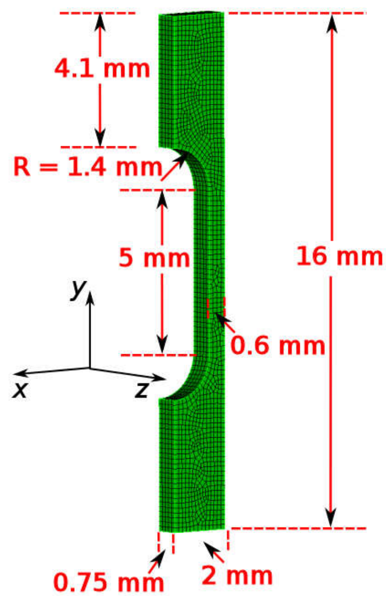

Figure 4. Dimensions of the half-geometry of the tensile specimen.

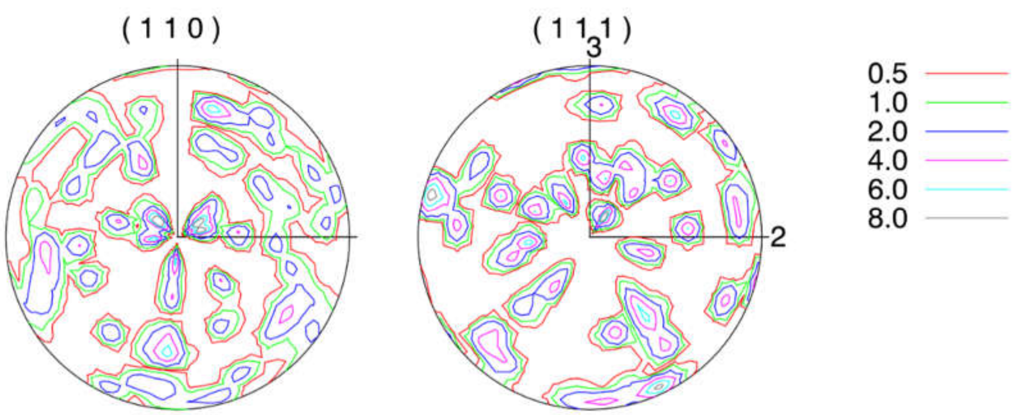

Figure 5. Randomly instantiated texture with 10 orientations.

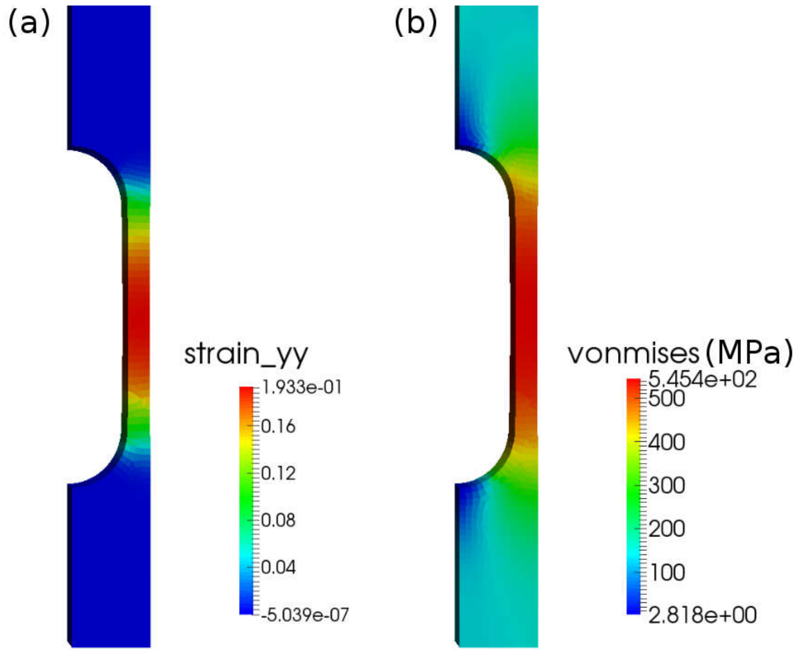

Figure 6. Distribution of (a) accumulated strain along the y-direction, and (b) von Mises stress in the specimen.

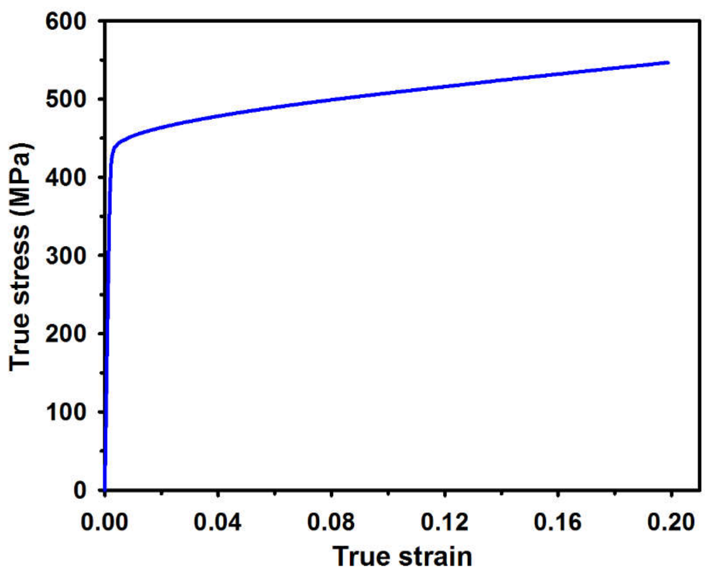

Figure 7. Simulated true stress-strain response of an element picked at random from the center of the gage section.

4.3. Effect of radiation dose on the deformation of a 3D bar specimen

We have performed tensile test simulations of a 3D bar specimen with different radiation dose histories. The bar specimen is 1 mm in length and 0.1 mm in breadth and width. The specimen was meshed using finite elements of uniform size 0.025 mm, such that there are a total of 640 elements in the simulation geometry. This simulation geometry is shown in Fig. 8(a). The bottom face of the specimen was constrained in the z-direction, and the center node of the bottom face constrained in all degrees of freedom to prevent rigid body motion. Bars with two different radiation dose histories were simulated: (a) the bottom end of the rod has 1.6 dpa radiation dose and the dose decreases along the length of the bar according to the profile shown in Case 1 in Fig. 8(b), and (b) a uniform radiation dose of 1.6 dpa across the length of the bar, as shown in Case 2 in Fig. 8(b). The same texture as in Fig. 5 was used in these simulations. Displacement-controlled loading was applied on the top face along the z-direction and the bars were loaded to a nominal strain of 10%.

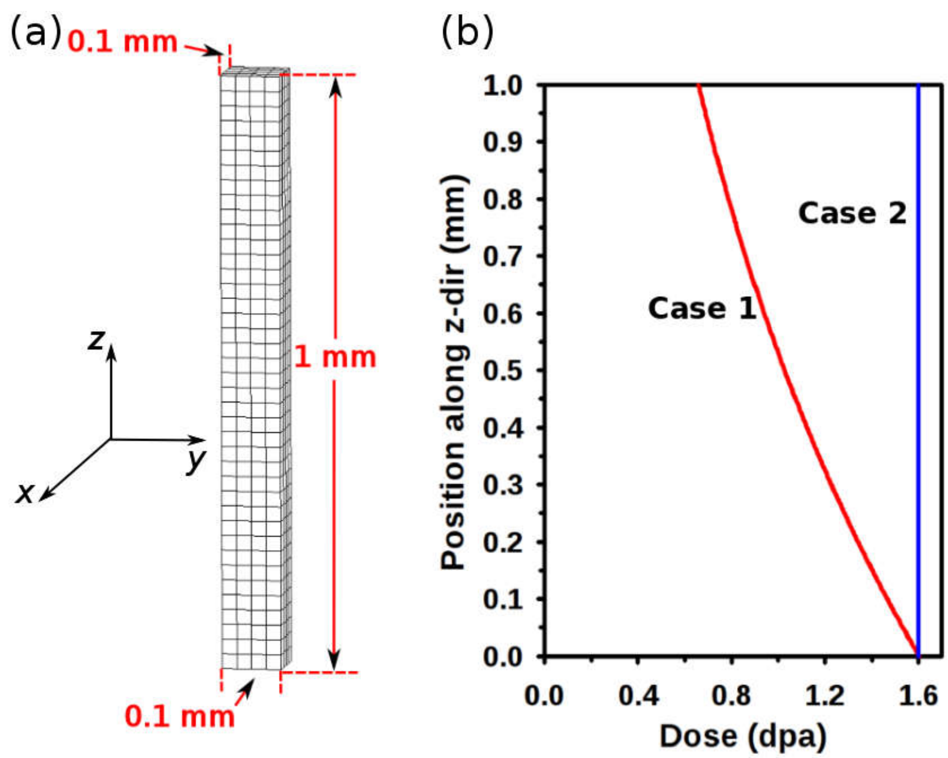

Figure 8. (a) Simulation geometry of the bar specimen, and (b) radiation dose histories along the length of the bar for two different cases.

The distribution of strain (along the z-direction) and von Mises effective stress for the two cases are shown in Fig. 9. It is seen that the bar with a variable radiation dose history (Case 1) has a heterogeneous deformation profile. Specifically, deformation is localized near the top end of the bar. The top end of the bar exhibits strain magnitudes as high as 0.25, while the strain magnitudes near the bottom end are less than 0.05. The top end of the bar, with lower radiation dose, is more compliant since it has relative lower irradiation hardening and yield stress. As a result, the top end of the bar accommodates a higher fraction of the applied deformation and, as a consequence, the top section shrinks more than the bottom section due to the Poisson effect. The hardening model leads to an increase in the dislocation density and so to an increase in the local flow stress, which reaches 750 MPa near the top end, higher than the 640 MPa at the bottom end, which has a higher irradiation dose. Increased localization at the top is to be expected for larger deformation.

The bar with a uniform radiation dose (Case 2) exhibits a relatively homogeneous deformation profile. There is some small heterogeneity near the ends of the bar. This is due to the 'non-random' 10 grain texture, which leads to a non-negligible component of shear deformation. We have verified the same using VPSC-SA calculations. If an 'ideal' random polycrystal, with larger number of grains, were used in these simulations, it would eliminate the observed shear deformation, albeit at the cost of higher computational costs.

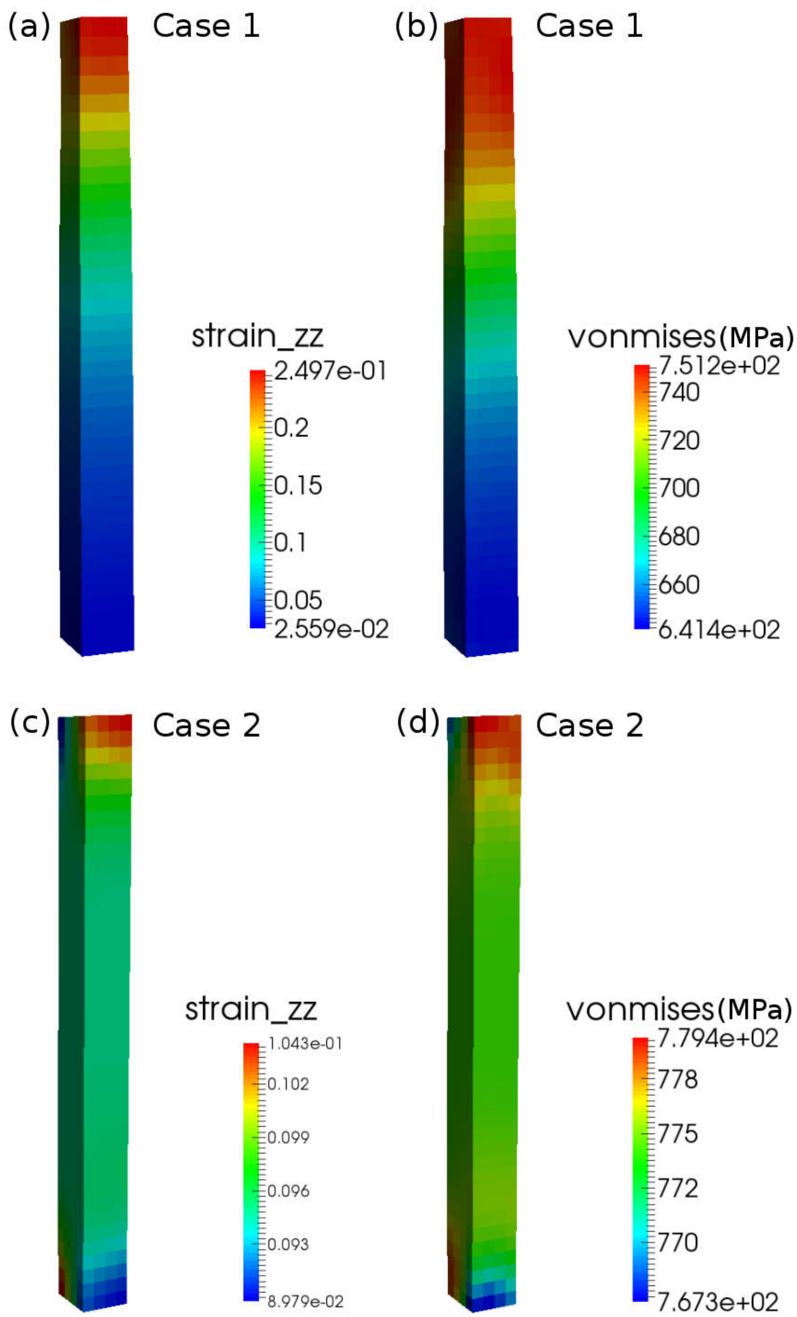

Figure 9. Distribution of (a) strain along the z-direction and (b) von Mises stress for Case 1, and (c) strain along the z-direction and (d) von Mises stress for Case 2. Note that the scales are different in each of these contours to highlight the heterogeneous deformation profiles.

5. Summary

The VPSC framework has been interfaced with the FE code, MOOSE to simulate irradiation hardening and plastic deformation in FeCrAl alloys in this work. This framework is validated by comparison of the stress-strain response predicted from VPSC-FE and VPSC-SA calculations. The framework is then used to simulate tensile deformation of a dog bone specimen. It is observed that majority of the deformation is accommodated in the gage section of the dog bone specimen. The framework is also used to study the effect of variable radiation dose on the deformation behavior of a bar specimen. The deformation tends to localize in regions of the bar with lower irradiation dose, which have relatively lower irradiation hardening and are more compliant.

References

[1] A. Patra, W. Wen, E. Martinez Saez, and C. Tome, "A defect density-based constitutive crystal plasticity framework for modeling the plastic deformation of Fe-Cr-Al cladding alloys subsequent to irradiation," Los Alamos National Laboratory, Los Alamos, NM, LA-UR--15-27896, 2016.

[2] A. Patra and D. L. McDowell, "Crystal plasticity-based constitutive modelling of irradiated bcc structures," *Philosophical Magazine*, vol. 92, no. 7, pp. 861–887, 2012.

[3] A. Patra and D. L. McDowell, "Continuum modeling of localized deformation in irradiated bcc materials," *Journal of Nuclear Materials*, vol. 432, no. 1–3, pp. 414–427, 2013.

[4] E. O. Hall, "The Deformation and Ageing of Mild Steel: III Discussion of Results," *Proceedings of the Physical Society. Section B*, vol. 64, no. 9, pp. 747–753, Sep. 1951.

[5] N. J. Petch, "The cleavage strength of polycrystals," *J. Iron Steel Inst.*, vol. 174, pp. 25–28, 1953.

[6] G. R. Odette and D. Frey, "Development of mechanical property correlation methodology for fusion environments," *Journal of Nuclear Materials*, vol. 85–86, no. Part 2, pp. 817–822, 1979.

[7] G. E. Lucas, "The evolution of mechanical property change in irradiated austenitic stainless steels," *Journal of Nuclear Materials*, vol. 206, no. 2–3, pp. 287–305, 1993.

[8] U. Essmann and H. Mughrabi, "Annihilation of dislocations during tensile and cyclic deformation and limits of dislocation densities," *Philosophical Magazine A*, vol. 40, no. 6, pp. 731–756, 1979.

[9] F. Roters, D. Raabe, and G. Gottstein, "Work hardening in heterogeneous alloys--a microstructural approach based on three internal state variables," *Acta Materialia*, vol. 48, no. 17, pp. 4181–4189, 2000.

[10] Y. Estrin and L. P. Kubin, "Local strain hardening and nonuniformity of plastic deformation," *Acta Metallurgica*, vol. 34, no. 12, pp. 2455–2464, 1986.

[11] R. A. Austin and D. L. McDowell, "A dislocation-based constitutive model for viscoplastic deformation of fcc metals at very high strain rates," *International Journal of Plasticity*, vol. 27, no. 1, pp. 1–24, 2011.

[12] R. A. Lebensohn, C. N. Tomé, and P. P. CastaÑeda, "Self-consistent modelling of the mechanical behaviour of viscoplastic polycrystals incorporating intragranular field fluctuations," *Philosophical Magazine*, vol. 87, no. 28, pp. 4287–4322, Oct. 2007.

[13] H. Wang, B. Raeisinia, P. D. Wu, S. R. Agnew, and C. N. Tomé, "Evaluation of self-consistent polycrystal plasticity models for magnesium alloy AZ31B sheet," *International Journal of Solids and Structures*, vol. 47, no. 21, pp. 2905–2917, Oct. 2010.

[14] *ABAQUS Version 6.14-1*. Dassault Systémes Simulia Corp., Providence, RI, 2014.

[15] J. Segurado, R. A. Lebensohn, J. LLorca, and C. N. Tomé, “Multiscale modeling of plasticity based on embedding the viscoplastic self-consistent formulation in implicit finite elements,” *International Journal of Plasticity*, vol. 28, no. 1, pp. 124–140, Jan. 2012.
[16] M. Knezevic, R. J. McCabe, R. A. Lebensohn, C. N. Tomé, C. Liu, M. L. Lovato, and B. Mihaila, “Integration of self-consistent polycrystal plasticity with dislocation density based hardening laws within an implicit finite element framework: Application to low-symmetry metals,” *Journal of the Mechanics and Physics of Solids*, vol. 61, no. 10, pp. 2034–2046, Oct. 2013.
[17] W. Liu, R. Montgomery, C. Tomé, C. Stanek, and J. Hales, “VPSC implementation in the BISON-CASL code for modeling large deformation problems,” in *ANS MC2015 - Joint International Conference on Mathematics and Computation (M&C), Supercomputing in Nuclear Applications (SNA) and the Monte Carlo (MC) Method*, Nashville, TN, 2015, pp. 1–15.
[18] A. Patra and C. Tome, “Interfacing VPSC with Finite Element Codes. Demonstration of Irradiation Growth Simulation in a Cladding Tube,” Los Alamos National Laboratory (LANL), Los Alamos, NM (United States), LA-UR--16-21960, Mar. 2016.
[19] R. D. McGinty, “Multiscale representation of polycrystalline inelasticity,” Georgia Institute of Technology, Atlanta, USA, 2001.
[20] K. G. Field, X. Hu, K. Littrell, Y. Yamamoto, R. H. Howard, and L. L. Snead, “Stability of Model Fe-Cr-Al Alloys Under The Presence of Neutron Radiation,” Oak Ridge National Laboratory (ORNL); High Flux Isotope Reactor (HFIR), 2014.
[21] K. G. Field, X. Hu, K. C. Littrell, Y. Yamamoto, and L. L. Snead, “Radiation tolerance of neutron-irradiated model Fe–Cr–Al alloys,” *Journal of Nuclear Materials*, vol. 465, pp. 746–755, 2015.